Mechanistic multiscale modelling of energy metabolism in human astrocytes reveals the impact of morphology changes in Alzheimer's Disease

Sofia Farina[1], Valérie Voorsluijs[2,3], Sonja Fixemer[2,4], David Bouvier[2,4,5], Susanne Claus[6], Mark Ellisman[7], Stéphane P.A. Bordas[1*], Alexander Skupin [2,3,7*]

1 Department of Engineering, University of Luxembourg, Esch-sur-Alzette, Luxembourg

2 LCSB-Luxembourg Centre for Systems Biomedicine, University of Luxembourg, Esch-sur-Alzette, Luxembourg

3 Department of Physics and Material Science, University of Luxembourg, Luxembourg, Luxembourg

4 Luxembourg Center of Neuropathology (LCNP), Dudelange, Luxembourg

5 Laboratoire national de santé (LNS), National Center of Pathology (NCP), Dudelange, Luxembourg

6 Onera, Palaiseau, France

7 Department of Neurosciences, University of California San Diego, California, United States of America

* stephane.bordas@alum.northwestern.edu SPAB, alexander.skupin@uni.lu AS

Abstract

Astrocytes with their specialised morphology are essential for brain homeostasis as metabolic mediators between blood vessels and neurons. In neurodegenerative diseases such as Alzheimer's disease (AD), astrocytes adopt reactive profiles with molecular and morphological changes that could lead to the impairment of their metabolic support and impact disease progression. However, the underlying mechanisms of how the metabolic function of human astrocytes is impaired by their morphological changes in AD are still elusive. To address this challenge, we developed and applied a metabolic multiscale

modelling approach integrating the dynamics of metabolic energy pathways and physiological astrocyte morphologies acquired in human AD and age-matched control brain samples. The results demonstrate that the complex cell shape and intracellular organisation of energetic pathways determine the metabolic profile and support capacity of astrocytes in health and AD conditions. Thus, our mechanistic approach indicates the importance of spatial orchestration in metabolism and allows for the identification of protective mechanisms against disease-associated metabolic impairments.

Author summary

Among the cells in our brain astrocytes are crucial to support neurons. Understanding the role played by astrocytes in neurodegeneration is of the utmost importance. In particular, the relationship between morphology and spatial metabolic arrangements requires further investigation since astrocytes present morphological changes and metabolic impairments in neurodegenerative diseases. We propose a computational metabolic model for better understanding the interplay between these two aspects of astrocytes. The model is solved in domains of increasing complexity from a two-dimensional circular domain to three-dimensional human astrocytes. The findings emphasise the importance of the spatial arrangement of metabolic reaction sites for the metabolic dynamics, which is further emphasised in the intricate structures of astrocytes where their morphological changes can be crucial for facilitating metabolic dysfunctions in neurodegeneration.

Introduction

The human brain is the organ with the highest energy demands required to sustain the high activity of neurons [1]. Astrocytes are multitasking glial cells directly contributing to brain homeostasis and metabolism. By their complex architecture as star-like branched cells, they are intermediate structures sitting between neurons and their synapses, which they enwrap with their intricate processes, and the blood vessels, which they contact with their endfeet. Based on this strategic positioning, astrocytes act as metabolic supporters providing energy in the form of lactate (LAC) to neurons and

modulating their activity [2,3]. While it is known that astrocytes provide neurons with lactate in high energetic demand, the hypothesis of astrocyte-neuron lactate shuttle (ANSL) [2] is an open debate [4,5]. Astrocytes are also known to respond to brain "trauma" and drastically change in many brain diseases such as Alzheimer's disease (AD). In these situations, they engage reactive profiles with changes in morphology and in their molecular program [6,7] like in AD where human astrocytes exhibit overbranching and context-dependent hypertrophy [8–11]. In addition to morphological changes, AD-associated astrocytes also exhibit metabolic dysfunctions [12–16], altering their role as neuronal supporters, but the relation to morphology is not established.

The metabolic support function of astrocytes depends on sufficient LAC production and efficient LAC export at the perisynapses as energy substrate for neurons [17] and on sufficient availability of adenosine triphosphate (ATP) for its own metabolic sustainability [18] requiring an ATP : ADP ratio at least larger than one [19]. Furthermore, physiological conditions for functional astrocytes are characterised by an approximate 10:1 ratio between LAC and pyruvate (PYR), the substrate for lactate production and mitochondrial activity, further indicating their metabolic support function [20]. Hence, astrocytes have to keep a balance between a LAC based "altruistic" support mode and a more "egocentric" self-sustainability characterised by a high ATP : ADP ratio. The mechanistic relationship between the observed disease-related modifications in morphology and metabolic dysfunctions is still to be characterised and whether morphology changes might represent a compensatory mechanism remains elusive.

Here, we develop a general interdisciplinary approach to systematically investigate the interplay between astrocytic morphology and energy metabolism in AD by a novel spatiotemporal *in silico* model that allows for physiologically realistic simulations by integrating complex morphologies obtained by high-resolution confocal microscopy and thereby addresses the impossibility of appropriate *in vivo* human astrocyte studies. Metabolic modelling has been extensively addressed in the literature at different levels *via* detailed genome-scaled metabolic network models [21] or *via* targeted dynamic models [22], including astrocytic metabolism [23–27]. All existing models neglect the spatial dimensions as they describe the metabolic processes through ordinary differential equations (ODEs). The underlying assumption that diffusion and reaction rates of

metabolism are large enough to smear out spatial aspects are challenged by the complex [41] morphology of astrocytes and an increasing amount of evidence for relocation of [42] enzymes and other reaction sites in different conditions [28, 29]. To include spatial [43] variations and geometric effects, we developed a metabolic model by means of a complex [44] reaction-diffusion system (RDS) in realistic three-dimensional (3D) morphologies [45] obtained from high-resolution confocal microscopy images of astrocytes in *post mortem* [46] brain samples of AD patients and age-matched control subjects [30]. The modelling [47] framework incorporates two essential astrocytic properties: 1) the main reactions of [48] glucose metabolism are spatially localised to reflect the heterogeneous distribution of [49] enzymes in the cell [28], and 2) the complex and context-dependent geometry of cells is [50] directly incorporated from high-resolution microscopy [10, 31]. To address the resulting [51] computational challenges in solving the corresponding partial equations of the RDS in [52] realistic astrocytic morphologies with thin branches and regions of high curvature and [53] kinks, we adapted our previous approach [32] utilising the power of the cut finite [54] element method (CutFEM) [33, 34] to disentangle the complex astrocytic geometries [55] from the mesh generation of finite-element methods and handle complex geometries as [56] independently of the mesh as possible. Compared to our previously proposed model, we [57] calibrated physiologically the parameters, investigated the spatial arrangements and [58] molecular diffusivity and include real astrocytic morphologies. [59]

By this approach, our model paves the way to more physiological modelling of the [60] effect of astrocytic morphology in AD. Our framework is general and open-source and [61] can be used for other cell types characterised by high-resolution imaging. For model [62] establishment, we first performed simulations in simple two-dimensional (2D) [63] geometries and studied how metabolic dynamics are affected by the spatial arrangement [64] of reaction sites. The findings in 2D indicated the importance of the spatial component [65] and the diffusion limitation that arises from the competition between the corresponding [66] reaction centers for the metabolic substrates. Furthermore, the results highlighted the [67] fundamental role of mitochondrial organisation for the metabolic output of the system. [68] Based on these insights, we subsequently investigated spatiotemporal metabolic [69] dynamics in real 3D human astrocytic morphologies by our multiscale modelling [70] approach and demonstrate the potential of our framework to study metabolic [71] dysfunction in AD-related reactive morphology of astrocytes. [72]

Results

To investigate the potential mechanistic link between morphology and energy metabolic activity, our model describes glucose metabolism by five main metabolic pathways (Fig 1A). Our proposed model prioritises a simple description of the chemical reactions to focus our study on the morphology and on the spatial component of the model. We describe glycolysis *via* two subsequent pathways where the first represents the ATP consuming and the second one the ATP producing reactions. The first pathway is catalysed by a set of enzymes (hexokinase, phosphoglucose isomerase, phosphofructose kinase and the fructose bisphosphate aldolase), which consume glucose (GLC) and ATP to produce ADP and glyceraldehyde 3-phosphate (GLY). In the following, we describe this pathway by a coarse-grained hexokinase (HXK) activity capturing the rate-limiting step of the glycolysis. In the second lumped reaction, these metabolites are transformed into ATP and pyruvate (PYR) by a second set of enzymes (glyceraldehyde phosphate dehydrogenase, phosphoglycerate kinase, phosphoglycerate mutase, enolase and pyruvate kinase), which we describe by the overall activity of the pyruvate kinase (PYRK), catalysing the irreversible step in the second part of the glycolysis. The generated PYR is subsequently metabolised into LAC by the lactate dehydrogenase (LDH) or used by mitochondrial metabolism to generate ATP. The mitochondrial metabolic activity of the Krebs cycle and oxidative phosphorylation is described by the coarse-grained effective reaction Mito. Finally, another effective reaction (act) accounts for various ATP-consuming processes associated with cellular activity. These metabolic pathways are put into a spatial context by distributing the corresponding reaction centers into a spatial domain.

Metabolic dynamics and reaction sites competition in 2D domains

For model establishment and calibration, we first analyzed the effect of different spatial arrangements of reaction sites on the metabolic profile in simple 2D geometries. For this, we considered a circular domain and compared different configurations of reaction locations. The diameter of the circular domain was set to $140\,\mu$m as an average diameter that contains a full astrocyte [35]. To reflect the metabolic flux from the

endfeet towards the perisynapses at the neurons' locations, we placed the entry of GLC and the exit of LAC at opposing sides of the circle (Fig 1B) where the subregions are defined as the intersection of a circle with a radius of $10\,\mu$m and centers are located at the origin for GLC and the antipodal point for LAC. The parameters used in the model are shown in Table 1 and sensitivity analysis can be found in S1 in S1 Text.

In this simplified setup, we first assumed that a given reaction occurs around a single location with a spatial extent of a Gaussian distribution with a width of $\sigma = 20.0\,\mu$m except for the cellular activity. Biologically, cellular activity might also vary spatially [2, 36], with a higher energy demand at the perisynapses where neuronal activity induces higher cellular activity such as by neurotransmitter uptake. However, here we mainly focus on the metabolic reactions and their spatial relevance. As a control case ("Control"), all four reactions were located in the center of the circle as shown in Fig 1C, mimicking a well-stirred condition. In a more complex enzyme arrangement, we located the four reactions on the vertices of an equilateral triangle inscribed inside the circle: one reaction is placed on the top vertex close to the LAC exit, one reaction on the bottom right vertex and two reactions are placed on the bottom left vertex. An example is shown as "Arrangement 1" in Fig 1B, where PYRK and LDH are placed on top of each other, while HXK and Mito are on the top and bottom right vertex, respectively. The choice of this setting is arbitrary and not biologically relevant, with the only purpose of showing that the spatial arrangement of reaction sites impacts the output of the system.

The resulting dynamics of the Arrangement 1 and the Control setup are shown in Fig 1D where the average concentration dynamics inside the domain for each involved metabolite are shown. As a reference, we also plotted the steady state concentrations from Cloutier *et al.* [24], which was used to calibrate parameters of our model for which no literature information was available (see Table 1). As expected, the Control configuration leads to steady-state concentrations in agreement with Cloutier *et al.* during an equilibrium period of ≈ 50s, with an exception for LAC which exhibits an almost doubled level. By contrast, the arrangement of the enzyme sites in spatially distributed configurations such as Arrangement 1 affects the metabolite levels of interest. For example, the steady-state corresponding to Arrangement 1 is characterised by concentrations of GLC, GLY, PYR and LAC that are approximately four, ten, two

Model parameters				
Parameter name	Value	Description	Units	Reference
D_{GLC}	$0.6E3$	diffusion coefficient of glucose	$[\mu\mathrm{m}^2\mathrm{s}^{-1}]$	[37]
D_{ATP}	$0.15E3$	diffusion coefficient of ATP	$[\mu\mathrm{m}^2\mathrm{s}^{-1}]$	[38]
D_{ADP}	$0.15E3$	diffusion coefficient of ADP	$[\mu\mathrm{m}^2\mathrm{s}^{-1}]$	[38]
D_{GLY}	$0.51E3$	diffusion coefficient of glyceraldehyde	$[\mu\mathrm{m}^2\mathrm{s}^{-1}]$	[39, 40]
D_{PYR}	$0.64E3$	diffusion coefficient of pyruvate	$[\mu\mathrm{m}^2\mathrm{s}^{-1}]$	[39, 40]
D_{LAC}	$0.64E3$	diffusion coefficient of lactate	$[\mu\mathrm{m}^2\mathrm{s}^{-1}]$	[39, 40]
$\mathrm{GLC}(t=0)$	0.0	initial concentration of glucose	[mM]	
$\mathrm{ATP}(t=0)$	1.6	initial concentration of ATP	[mM]	[24]
$\mathrm{ADP}(t=0)$	1.6	initial concentration of ADP	[mM]	
$\mathrm{GLY}(t=0)$	0.0	initial concentration of glyceraldehyde	[mM]	
$\mathrm{PYR}(t=0)$	0.0	initial concentration of pyruvate	[mM]	
$\mathrm{LAC}(t=0)$	0.0	initial concentration of lactate	[mM]	
J_{in}	0.048	influx of glucose	$[\mathrm{mM}\,\mathrm{s}^{-1}]$	[24]
J_{out}	0.0969	degradation term of lactate	$[\mathrm{s}^{-1}]$	[24]
K_{HXK}	$6.19E-02$	reaction rate of hexokinase	$[(\mathrm{mM})^{-2}\mathrm{s}^{-1}]$	[24]
K_{PYRK}	1.92	reaction rate of pyruvate kinase	$[(\mathrm{mM})^{-2}\mathrm{s}^{-1}]$	[24]
K_{Mito}	$8.13E-02$	reaction rate of mitochondria activity	$[(\mathrm{mM})^{-28}\mathrm{s}^{-1}]$	[24]
K_{act}	$1.69E-01$	reaction rate of cellular activity	$[\mathrm{s}^{-1}]$	[24]
K_{LDH}	$7.19E-01$	reaction rate of lactate dehydrogenase	$[\mathrm{s}^{-1}]$	[24]

Table 1. Model parameters

and three times higher compared to the well-mixed condition described by ODEs in   135
Cloutier *et al.*, respectively.   136

The steady-state solutions of Arrangement 1 indicate the necessity of the species to   137
diffuse inside the domain and reach the corresponding enzyme sites: GLC needs to   138
diffuse into the other part of the domain to act as a substrate for HXK, and the   139
produced GLY needs to reach the PYRK to be metabolised into PYR. The reactions   140
are thereby diffusion-limited and the system reaches the steady state before consuming   141
more GLY. Finally, the increased LAC level for Arrangement 1 in relation to the   142
Control is caused by the co-localisation of PYRK and LDH where produced PYR is   143
directly metabolised into LAC whereas in the Control, Mito and PYRK compete for   144
PYR as substrate.   145

146

To investigate systematically the effect of co-localisation and/or proximity of   147
reaction centers to GLC influx or LAC efflux, we considered all possible location   148
configurations for the four reactions on the vertices of the triangle (Fig 1B). Considering   149
the colocalisation of two reactions in the left-bottom vertex leads to twelve possible   150
location configurations (Fig 2A and 2C). As a first attempt to address slightly more   151
complex morphologies, we studied the twelve arrangements within a two-dimensional   152
star shape (Fig 2B) as a simplified version of an astrocyte. This setup allows for   153
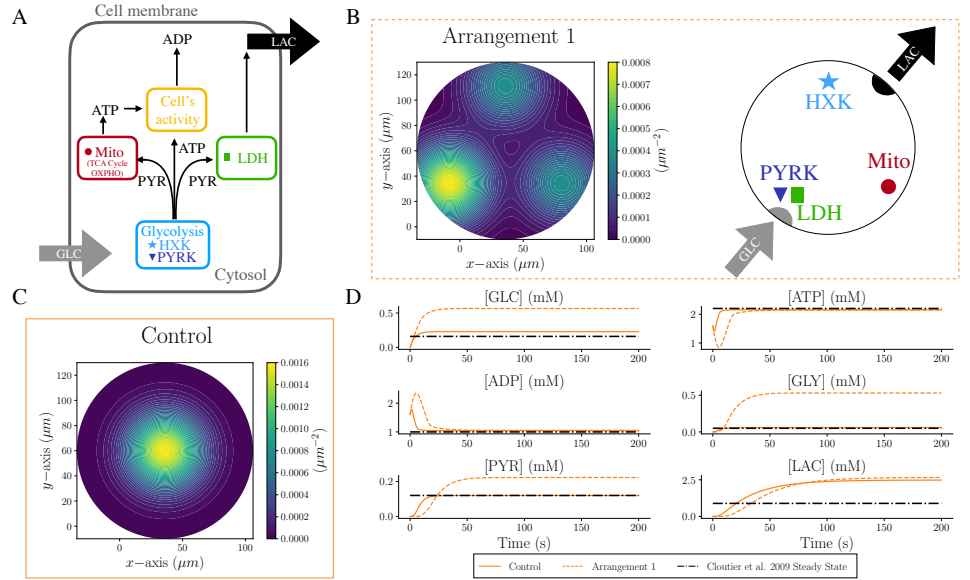
Fig 1. Spatial arrangement of metabolism has an impact on cellular metabolite concentrations.

A: GLC enters the cytosol of the cell and takes part in glycolysis whose effective kinetics is captured by the two reactions HXK and PYRK. The products of glycolysis are subsequently consumed by the LDH reaction for generating LAC, by the act reaction describing ATP consumption due to cellular activity, and by mitochondria where the effective reaction Mito produces ATP from PYR through the Krebs cycle and oxidative phosphorylation. B: (left) Generic configuration to investigate the effect of metabolite transport on the output of metabolism in a 2D circular domain. The color map highlights the position of the reaction sites (defined by $\sum_i \mathcal{G}(\mathbf{x}_i, \sigma_i) \quad i = \{\text{HXK}, \text{PYRK}, \text{Mito}, \text{LDH}\}$), which are located on the vertices of an equilateral triangle. Two reaction sites are colocalised at the bottom left corner. (Right) Position of the reaction sites in Arrangement 1: HXK on the top close to the efflux of LAC, PYRK and LDH colocalised close to the GLC influx, and Mito on the last vertex. C: Control scenario: all reaction sites are located in the center. D: Dynamics of the average concentration of each species in Arrangement 1 and Control, compared with the steady-state values from Cloutier *et al.* [24]

comparable results between the two domains since molecules have to pass similar distances between the subregions where GLC enters and the subregion where LAC is exported. Reaction sites were located analogously at the three vertices of an equilateral triangle within the star. As in the circular setup, we placed two reaction sites colocalised closer to the influx of GLC, and one reaction site at each of the remaining vertices.

Fig 2D shows the steady-state and spatially averaged concentration of each species of interest for the twelve possible configurations of the circular (left columns) and the star domain (right columns) where the maximum and minimum values for each species are highlighted in red and blue, respectively. Simulations performed in both domains exhibit similar trends. The species that are affected the most by the different spatial arrangement are GLC, GLY and PYR for the co-localisation of the reaction sites HXK-PYRK (Location 6 and 9) and PYRK-LDH (Location 1 and 4) which led to low level of GLY or PYR, respectively. In the Control, where all the reaction sites overlap in the center of the domain, the system is more efficient with low levels of GLC, GLY and PYR, and a medium value of LAC. Although LAC shows differences depending on the location of the reaction sites, the changes are less significant due to the efflux which reduces LAC steady-state concentrations. Interestingly, the star-shape domain exhibits the highest values of LAC pointing to the importance of morphologies with branches and higher complexity. Since cellular activity is assumed to occur homogeneously inside the domains, variability in ATP and ADP levels across the setups are rather small confirmed by the [ATP] : [ADP] ratio with a variance between all the simulations of $0.005 \, (\mathrm{mM}^2)$ (Fig 2E).

Overall, this *in silico* experiments emphasise the variable output of the metabolic RDS as a function of the intracellular spatial organisation of reaction sites. To further investigate this effect, we next modelled the effect of enzyme distributions in more detail.
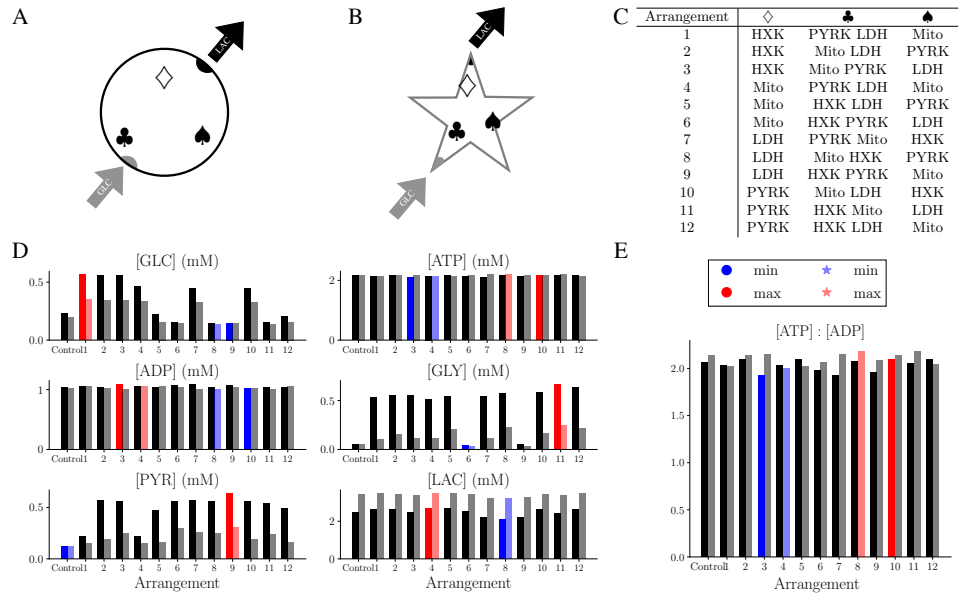
Fig 2. Spatial organisation and competition between reaction sites affect the metabolic activity of the system.

A: Spatial setting of simulations performed in a 2D circle. GLC enters along one side, and on the diametrically opposite side, LAC is exported. Each of the three symbols is associated with one (diamond and spade) or two (club) reactions. B: The spatial setting of simulations performed in the star shape. The reaction sites are located analogously to the circle domain with the same distance between the GLC entry vertex and the LAC efflux/degradation. C: Table of the 12 possible configurations corresponding to the allocation of one reaction site to diamond and spade vertices, and two colocalised reaction sites at the club vertex. D: Spatially averaged steady-state concentrations of each species for the circle (left in black) and the star (right in grey) E: Spatially averaged steady state ATP : ADP ratio for simulations in a circular (left in black) and star-like geometry (right in grey).

Uniform and polarised distribution of reaction sites in a rectangular domain

Based on the establishment of the spatiotemporal metabolic model for one reaction center for each pathway reaction, we next explored the effect of inhomogeneous distributions of reaction centers on the metabolic state of the cell. For this purpose, we considered for each metabolic reaction ten distinct reaction sites with a smaller spatial extent ($\sigma = 1.0\,\mu$m), while conserving the overall metabolically activity. To mimic the morphology of astrocytic branches, the shape of the RDS domain was chosen as a two-dimensional rectangle of dimension $[0, l] \times [0, L]$, with width $l = 4\,\mu$m and a length $L = 140\,\mu$m [35] where GLC enters from the bottom left corner of the rectangle (origin) and LAC exits from the top right corner. We considered two types of cellular organisation: one where the reaction sites are uniformly distributed inside the domain and the extreme opposite setting of a polarised cell where some reactions occur predominantly at one of the extremities of the cell. The polarised cells are a set of configurations representing an extreme enzymatic setting, which might not be physiologically relevant but allows us to isolate and test a mechanistic hypothesis. In other words, using extreme (and hence rather arbitrary) configurations is a way to validate a mechanism while avoiding the perturbations attributed to competing processes. To ensure the robustness of the findings, the two settings were compared by ensemble simulations of 200 distinct realisations of each setting. For the uniform cells, the coordinates of the 10 reaction sites of each type were randomly selected from a uniform distribution that covers the rectangular domain. realisations of polarised cells were generated either by normal distributions ($\mathcal{N}(m, \sigma')$, where m and σ' denote the mean and standard deviation, respectively) or by log-normal ($\log\mathcal{N}(m, \sigma')$) distributions. Fig 3A shows the position of the reaction sites along the y coordinate of the 200 realisations and Fig 3B exemplifies enzyme distributions for a given cell for each setting. The different strategies for polarised cells lead to a certain probability for mitochondria localisation in the upper part of the domain for the "Polarised" configuration but not for the "Polarised $\log\mathcal{N}(2)$" configuration (Fig 3A). These settings allow for investigating the competition between the Mito and LDH reactions for their shared substrate PYR (S2 in S1 Text). In fact, the two kinds of polarised cells

have been chosen to investigate the effect of different mitochondria locations. The 212
glycolytic reactions are close to the influx to mimic the most efficient consumption of 213
the glucose entering the cell, while the lactate dehydrogenase located on the opposite 214
side of the domain allows the investigation of how the substrate pyruvate diffuses inside 215
the domain and encounters first the Mito and then the LDH reactions. 216

217

To assess the effect of the different spatial arrangements, the steady state 218
concentration of the 200 realisations, for the three different configurations, were 219
compared statistically (Fig 3C) including T-test and Wilcoxon-Mann-Whitney with 220
Holm-Bonferroni compensation (the corresponding table is shown in S3 in S1 Text). 221
The p-value results show that only GLY for the uniform and polarised cell, and PYR 222
for the two polarised configurations are not significantly impacted by the spatial 223
arrangements where GLY exhibits a high $p-$value only in the t-test (0.093) but not in 224
the non-parametric one. This finding is consistent with the similar average of the 225
steady-state concentration but the distinct underlying distribution (Fig 3C). For PYR, 226
the distributions for the two polarised cells exhibit a similar range (Fig 3C). However, 227
since the two polarised cells only differ by the distribution of mitochondria it is expected 228
that the distribution of PYR is similar because it is produced in PYRK reaction. 229
In general, the polarised cells consume more GLC than the uniform distributed ones, 230
which is consistent with the fact that the reaction HXK is closer to the influx. GLY is 231
present at a very low level for all configurations as also shown in the significance test. 232
Interestingly, PYR and LAC differ strongly in polarised cells compared to the uniform 233
setting with a higher level in PYR caused by faster metabolising of GLC by the HXK 234
and subsequent PYRK reactions. On the other hand, LAC levels are higher for the 235
uniform cells since in polarised cells PYR reaches the more distant LDH reaction only 236
by the amount which has not been consumed by the closer located Mito reactions. The 237
resulting LAC : PYR concentration ratios for the cells with uniformly distributed 238
enzymes respect the physiological constraints, whereas polarised cells exhibit ratios 239
below one indicating an unphysiological or diseased state. 240
The corresponding ATP and ADP concentrations show a rather low variability for 241
the uniform configuration with higher ATP and lower ADP concentrations (Fig 3C) 242
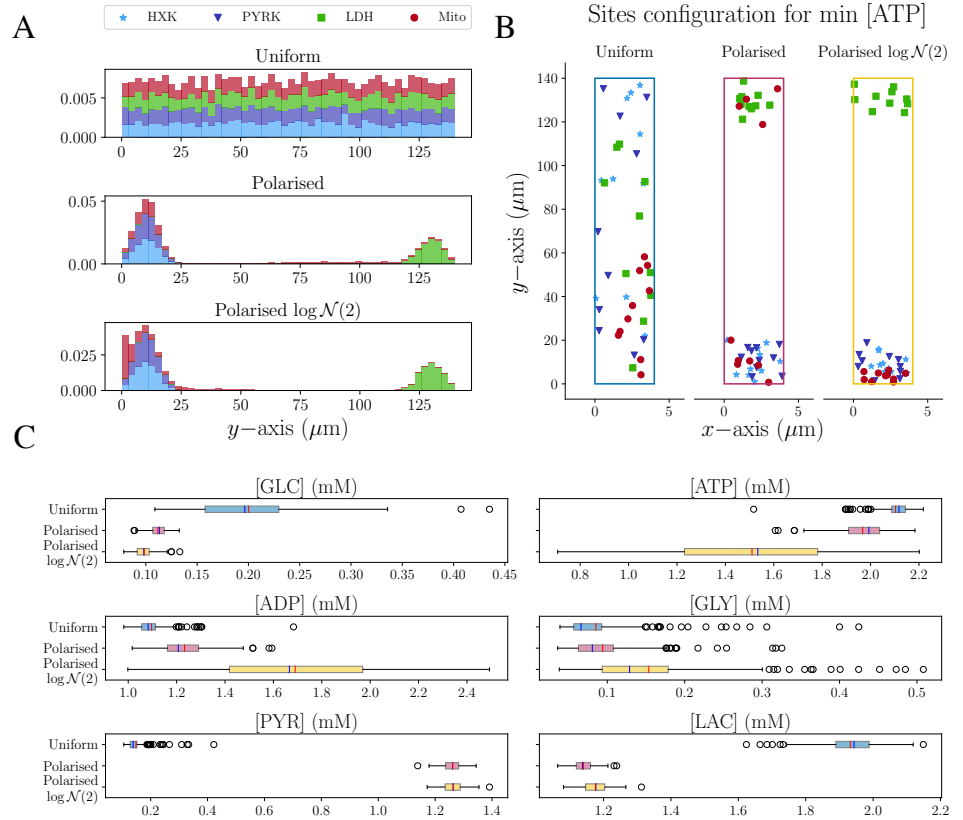
Fig 3. The steady-state level of metabolites is affected by the polarised distribution of enzymes within cells.

A: Distribution of the reaction sites along the y-axis of the rectangular domain where the data are stacked on top of each other for visibility: HXK in light blue, PYRK in dark blue, LDH in green and Mito in dark red (top panel). In the Uniform setting, the reacting sites are uniformly distributed along the y-axis. In the Polarised settings, HXK, PYRK and LDH are spread unevenly over the domain with the first two located close to the origin and the latest close to the top of the domain. Mito reaction sites are distributed in the following way: 6 of them are normally distributed and colocated in the same area as HXK and PYRK, and 4 of them are uniformly located in the upper part of the domain (middle panel). In the Polarised $\log \mathcal{N}(2)$ setting, mitochondria are located in the domain according to a log-normal distribution (bottom panel). B: Examples of Uniform, Polarised and Polarised $\log \mathcal{N}(2)$ distributions for the less energised cell where mitochondrial production is the most affected by polarisation. C: Box plot of the average steady-state concentration of each species for the Uniform, Polarised and Polarised $\log \mathcal{N}(2)$ distributions. (The mean and median of each box are signed in red and blue, respectively.)

compared to the polarised cells. Interestingly, the Polarised $\log\mathcal{N}(2)$ configuration exhibits a very wide range for both concentrations with significantly different average values also in comparison with the Polarised configuration. Since the only significant difference between the Polarised and Polarised $\log\mathcal{N}(2)$ configurations lies in the distribution of mitochondria inside the domain (red bars in middle and bottom panels of Fig 3A), we conclude that the difference in the cellular energetic state can only be attributed to the location of mitochondria within the cell. Furthermore, the ATP : ADP ratio for the three cellular configurations (Fig 4A) confirms that the Polarised $\log\mathcal{N}(2)$ realisations cover an ATP : ADP ratio range from unhealthy (ratio < 1) to healthy (ratio ≥ 1).

The impact of the configurations on the metabolic activity and in particular with a focus on the "altruistic" behaviour producing more LAC or an "egocentric" strategy producing more ATP, can be visualised by the relationship between LAC and the ATP : ADP ratio (Fig 4B). We found two distinct clusters formed by uniform and polarised cells, where the uniform cells display a co-existing egoistic and altruistic mode characterised by high ATP and LAC concentrations for self-sustainability and neuronal support. Indeed, the correlation between the variables, the ratio and LAC, is only slightly negative for the uniform cells (-0.19), whereas the group of polarised cells exhibits a stronger negative correlation (-0.65) indicating that high values of one quantity lead to low values of the other. "Polarised" cells are located on the top of the cluster and the "Polarised $\log\mathcal{N}(2)$" cells are predominantly in the lower part of the cluster characterised by a lower ATP : ADP-ratio and slightly higher LAC concentrations (Fig 4B). This difference indicates the importance of mitochondria localisation as shown by the color-indicated classification of the vertical arrangement of mitochondria. We colored the metabolic profile of each realisation based on the highest y−coordinate of Mito sites ($y_{\max}$): yellow, orange, red or black, if $y_{\max} < 30$, $30 < y_{\max} < 60$, $60 < y_{\max} < 100$ or $y_{\max} > 100$, respectively. This analysis highlights that the lowest level of ATP coincides with realisations where all mitochondria are grouped in the lower region. By contrast, simulations with a high energetic profile correspond to arrangements where mitochondria are distributed throughout the whole rectangular shape. Fig 4C-4D show the mitochondrial spatial arrangement for the most energised cells and the corresponding mitochondria activity at the steady state. Not all
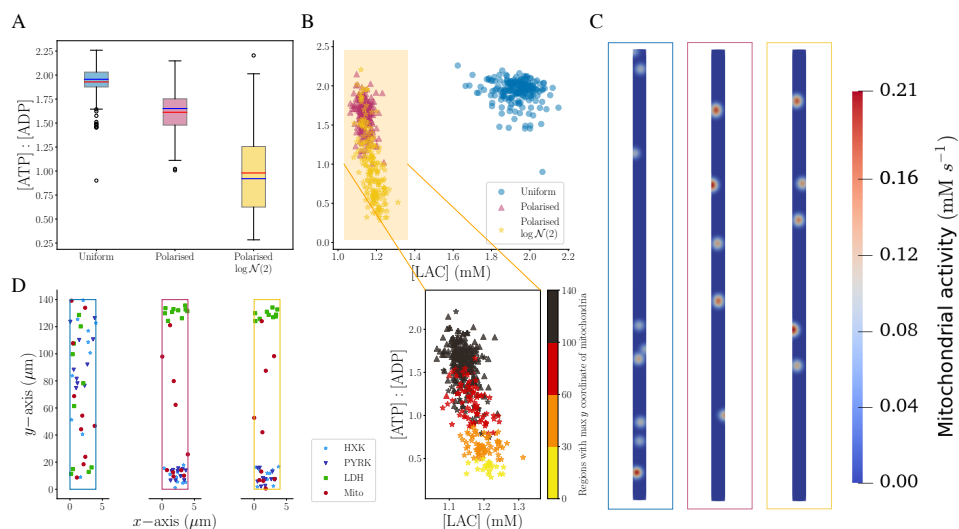
Fig 4. Mitochondrial distribution determine [ATP] : [ADP] **ratio and thereby energetic states of cells.**
A: Box plot of the final average values of the [ATP] : [ADP] for Uniform, Polarised and Polarised $\log \mathcal{N}(2)$ (Mean in red and median in blue). B: (top) scatter plot of the ratio against LAC final average values. There are two distinct clusters between the Polarised cells and the uniformly distributed ones. (bottom) Zoom on the ratio against LAC for Polarised cells colored based on the region where we can find the mitochondria with the highest y-coordinate. Interestingly if the enzymes are well distributed inside the domain, so if there is at least one mitochondria with a y-coordinate larger than 100 (black), the ratio value is higher. On the other hand, if the mitochondria are all located within the first or second region (yellow and orange), with y-coordinate lower than 60, the cell is in unhealthy status. C: Mitochondria activity of the configurations with maximum ATP production for the three types of cells at steady state where the activity indicates which mitochondria between the ones presented in panel D are producing ATP. D: Reaction sites setting for the maximum level of ATP for the three distributions.

mitochondria shown in the spatial arrangements are active at the steady state. Their   275

activity relies on the availability of ADP to produce ATP. For this reason, the   276

mitochondria located in the lower part of the Polarised cells are not active (more in S4   277

in S1 Text). Hence, the mitochondria activity for these arrangements remarks the   278

necessity of mitochondria to be well-distributed in the whole domain to sustain high   279

ATP levels. The importance of having Mito reactions uniformly distributed inside the   280

domain lies in the fact that Mito requires ADP as a substrate to be activated. However,   281

the non-uniform distribution of the reaction sites, for example, the ones of the less   282

energised cell with minimum ATP shown in Fig 3B, generates regions with a high   283

gradient of ADP or ATP (more in S4 in S1 Text).   284

285

Overall, this analysis demonstrates the impact of the interplay between spatial enzyme orchestration and morphology on the metabolic profile of cells. Our finding highlights that different cellular organisation leads to different steady-state concentrations which might be linked to potential disease of cells.

Morphological effects on the metabolic activity of human astrocytes in health and AD

Finally, we extend our work to 3D reconstructions of human astrocytes acquired from GFAP-immunostained *post-mortem* brain samples from age-matched control subjects (Fig 5A- 5C) and AD patients (Fig 5D-5F). The 3D confocal images of the astrocytes were acquired in the CA1 subregion of the hippocampus (Fig 5A and 5D). Given the typical *post-mortem* nature of such brain samples, the dynamical consequences of the morphology for metabolic profiles can be only assessed by an appropriate *in silico* strategy. The respective segmentations of the prototypical astrocytes (Fig 5B and 5E) reveal significant differences in the volume and morphological diversity of the two cells: the reactive AD astrocyte exhibits hypertrophy [10], proliferation of branches and coverage of wider spatial domains in comparison with the less complex shape of the control astrocyte (Fig 5G and 5H). Based on mitochondria staining and segmentation (Fig 5A- 5B and Fig 5D- 5E), a realistic spatial arrangement of mitochondria is implemented in the multiscale model (Fig 5C and 5F). The presence of regions with different mitochondrial densities is respected by tuning the center positions and variances of the Mito spatial reaction rates (Fig 5C and 5F). The minimum variance is set to $1.0\,\mu$m and we scale accordingly the size of the other regions with a maximum of $2.0\,\mu$m. The number of reaction sites for the other reactions is set according to the amount of mitochondria selected from post-processing, 97 for the control and 140 for the reactive astrocyte (Fig 5I). For each Mito reaction site, we located a HXK site close by in agreement with the observed relationships between these two enzymes [41, 42]. The reaction sites of PYRK and LDH are taken from a uniform distribution defined in the three-dimensional box containing the astrocyte. The locations of the reaction sites for the simulations inside the control and AD reactive astrocyte are shown in Fig 6A and 6C together with the assumed endfeet for GLC influx and the subregions at the
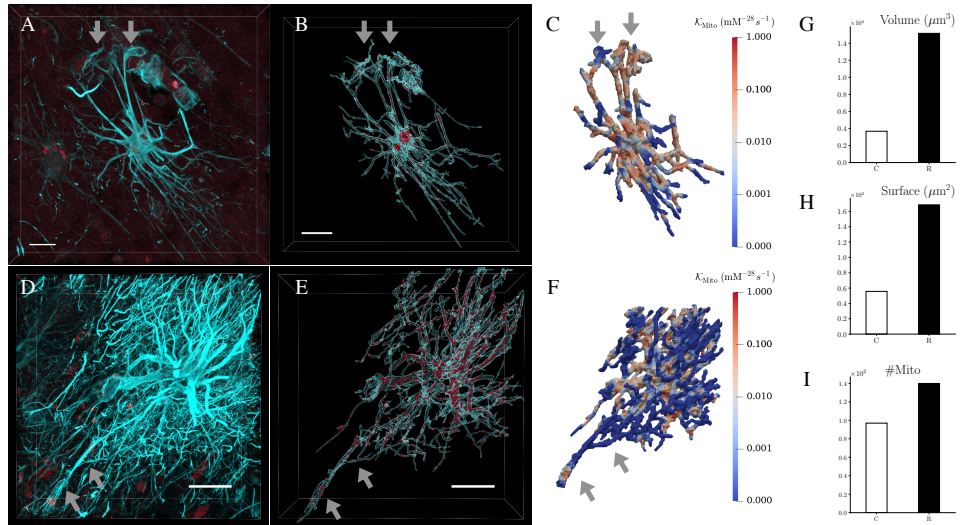
Fig 5. Human hippocampal astrocytes from an age-matched control subject and AD patient: from microscopy image to 3D simulation setting.
A and D: High-resolution confocal microscopy images from an age-matched control subject (panel A) and from an AD patient (panel D) were obtained from $50 - 100\,\mu$m brain sections that were immunostained against GFAP (cyan) to visualise astrocyte cytoskeletal morphology, and against TUFM (dark red) to reveal mitochondria in the hippocampuswhere the grey arrows indicate the endfeet of the two astrocytes in accordance with the blood vessels locations. B and E: Using Imaris 9.6.0, astrocyte 3D morphology was segmented using the surface tool and mitochondria were labelled with the spots tool for the astrocytes in both conditions. Finally, based on the segmentation, we created the domains for our simulations and we selected the locations with higher density to define the Mito reactions. C and F: Spatial reaction rates $\mathcal{K}_{\mathrm{Mito}}$ describing the mitochondria activity inside the cells. In the bar charts, we compared G: the cell volumes – $3673\,\mu$m^3 for the control astrocyte (C) and $15161\,\mu$m^3 for the reactive (R), H: cell surfaces – $5569\,\mu$m^2 for (C) and $16854\,\mu$m^2 for (R), and I: the number of mitochondria activity centers – 97 for (C) and 140 for (R) computed in panel C and F. Scalebars: A-B $15\,\mu$m, D-E $30\,\mu$m.

perisynapses for LAC export into the extracellular space (Fig 6A- 6C). Since astrocytes are in contact with thousands of neurons [43] providing them with lactate, it would be biologically more accurate to consider multiple regions where lactate can exit the astrocyte [44]. In S5 in S1 Text, we provide additional experiments where we show the effect of considering more lactate exit sites and an increased cellular activity in the perisynaptic regions [2,36]. However, in this section, we remain consistent with the previous experiments considering only a polarisation of the cell with lactate export regions on the opposite side of the glucose influx and a homogeneous cellular activity.

As a first analysis, we ran three baseline simulations based on the physiological

parameters (Table 1) with one simulation inside the protoplasmic control morphology $_{326}$
(C) (Fig 6A), one within the same morphology but with a polarised distribution of $_{327}$
reaction centres (P) (Fig 6B) and one inside the reactive astrocyte (R) (Fig 6C, more $_{328}$
details are given in S6 in S1 Text). The resulting dynamics of these baseline simulations $_{329}$
(Fig 6D) are in good agreement with the investigation of enzyme distributions in the 2D $_{330}$
domains where scenarios C and R resemble properties of the uniform distributed cell $_{331}$
and P corresponds to the polarised cell (Fig 3B). However, the average LAC $_{332}$
concentration is higher than expected for P and lower than expected for C and R. Also $_{333}$
the PYR concentration is closer to that of the uniform setting for the P configuration. $_{334}$
While the concentration values of C and R are on average very close (Fig 6B), smaller $_{335}$
differences are visible mostly in GLC and LAC and attributed to the effect of the $_{336}$
morphological differences and reaction site configurations. $_{337}$

$_{338}$

To investigate a reactive astrocyte subject to AD, we extended our simulations by $_{339}$
gradually adding AD-related dysfunctions. Experiment 1 (E1) mimics a loss of GLC $_{340}$
uptake [45] by a 30% decreased GLC influx. Experiment 2 (E2) includes the $_{341}$
dysfunction in mitochondrial activity [46–48] inducing a lower ATP production by a $_{342}$
reduced reaction rate for Mito ($K_{\mathrm{Mito}}10^{-5}$). In accordance with available experimental $_{343}$
data [12], we considered an increment of the activity of LDH by a factor of ten in $_{344}$
Experiment 3 (E3) and an increment in the glycolysis rate in particular in the PYRK $_{345}$
reaction, also by a factor of ten in Experiment 4 (E4). In the final experiment (EAD), $_{346}$
all four conditions were combined to explore their possible synergistic effects. $_{347}$

Fig 7A exhibits the percentage of the concentration loss at steady state for $_{348}$
experiments E1, E2, E3, E4 and EAD compared to R. Interestingly, the 30% reduction $_{349}$
in GLC uptake in E1 is reflected by the final steady state in GLC ($\approx 28.7\%$ loss) which $_{350}$
induced a loss of $\approx 35\%$ in GLY, PYR and LAC. Dysfunctional Mito reactions lead to $_{351}$
an increase in the final GLC level and a loss in ATP and GLY whereas the level of LAC $_{352}$
is not affected. The experimentally observed increased activity of LDH (considered in $_{353}$
experiment E3) results mainly in faster metabolising of PYR. On the other hand, GLY $_{354}$
consumption is maximised by the turnover of PYRK in the E4 experiment while the $_{355}$
other concentrations are not affected. The combined effect of the individual $_{356}$
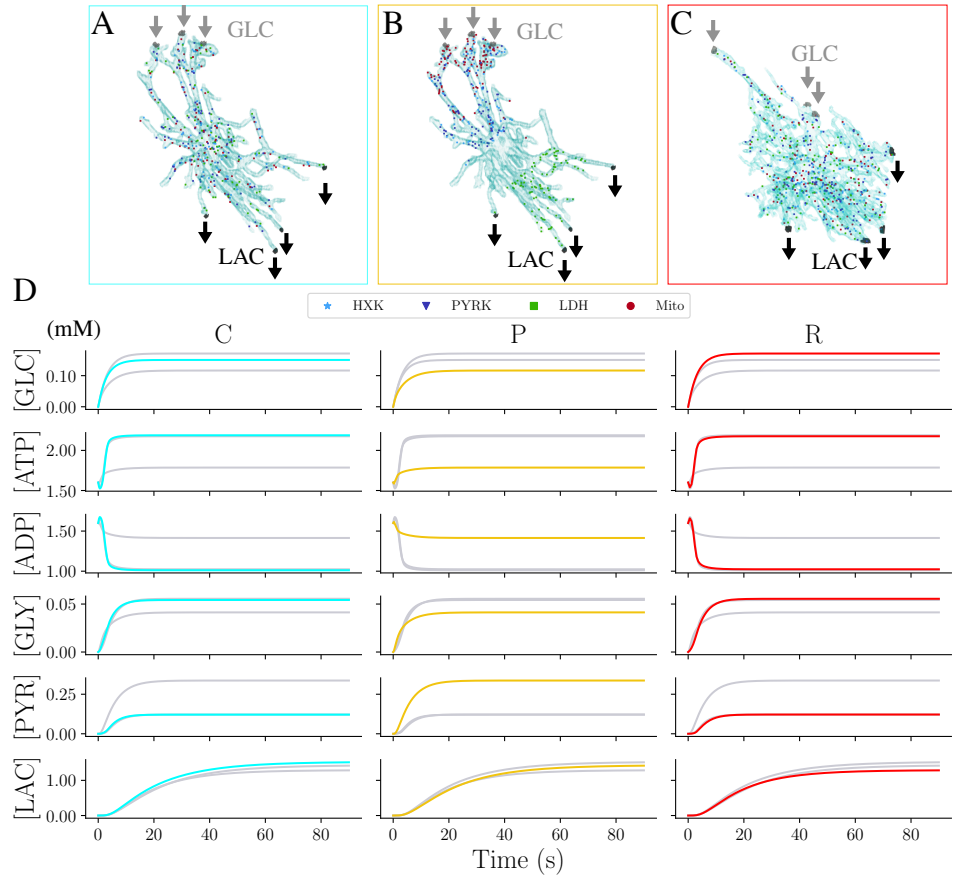
Fig 6. Metabolite dynamics in 3D astrocytes with physiological reaction site versus extreme polarised arrangements.

Setting of the 3D simulations for the A: control (C), B: polarised (P) and C: reactive (R) astrocyte. For C and R, Mito reaction centers were inferred from the microscopic images. Each HXK site is sorted from a gaussian distribution centered at each Mito site. In this way, for each Mito we have an HXK reaction close by. PYRK and LDH are uniformly distributed inside the box that contains the cells. The reaction centers of P are sorted in the way that HXK and PYRK are colocalised close to the GLC influx, while on the other extremity of the cell, we locate LDH centers. Mito centers are sorted using a log-normal distribution that locates them in the same region as HXK. The number of centers per reaction type is 90 for C and P, and 140 for R. For the three settings, GLC enters three sub-regions from the branches of the cell in contact with the blood vessels and LAC exits from four sub-regions at the other extremity of the cell. D: Time behavior of the average concentration of each species for C (cyan), P (yellow) and R (red).

dysfunctions in the EAD experiment leads to a significant change in the metabolic profile (with the highest loss in ATP, GLY and PYR Fig 7A). (The dynamics of these experiments are shown in S7 in S1 Text.)

The functional state of cells in terms of ATP : ADP and LAC : PYR ratios at steady state is preserved for a wide range of conditions. Even for the polarised P configuration, the ATP : ADP ratio is higher than 1.0 (Fig 7B and 7C), suggesting that a complex shape makes the cell more robust against extreme situations. This is also confirmed by the ratios of the E2 experiment, which does not exhibit a ratio below 1.0 despite mitochondrial dysfunction. The only cell that reaches a critical unhealthy state is the EAD condition (0.93), where mitochondrial dysfunction adds to the other dysfunctions. Also, the ratio of LAC : PYR is always within the physiological range (> 10) for all conditions except P. However, a LAC : PYR ratio of above 80 is reported in E3 and EAD, which may indicate hypoxia with low levels of oxygen in blood [20].

Since LAC export into the extracellular space is an essential mechanism of astrocytic support to neurons, we also quantified LAC efflux exporting LAC from the corresponding subregions (Fig 7D). The asymptotic behaviour of the efflux indicates that cells with the C and P configuration export more LAC, suggesting that the less ramified morphology of the protoplasmic astrocyte allows for faster diffusion of molecules and subsequent export regions. On the other hand, E1 and EAD configurations export less, indicating that the 70% decrease in GLC uptake might drive this AD symptom. The different metabolic states of the cell are also assembled in the "altruistic" vs "egocentric" map in terms of the LAC concentration and the ATP : ADP ratio (Fig 7E). This map indicates the C configuration as the most efficient cell with high levels for both in agreement with the previous finding on uniform distributed cells. The P setup exhibits a more altruistic behaviour than expected by producing more LAC than ATP, potentially facilitated by the morphology. When cells lack GLC, they become more egoistic and produce more ATP. Remarkably, the steady state of LAC of the R, E2, E3 and E4 experiments is $\approx 1.3\,\mu$M but the ATP concentration is decreasing from high levels in the R and E4 configuration to lower concentration in E2. Finally, lower levels of both ATP and LAC are the AD-related EAD condition suggesting that it
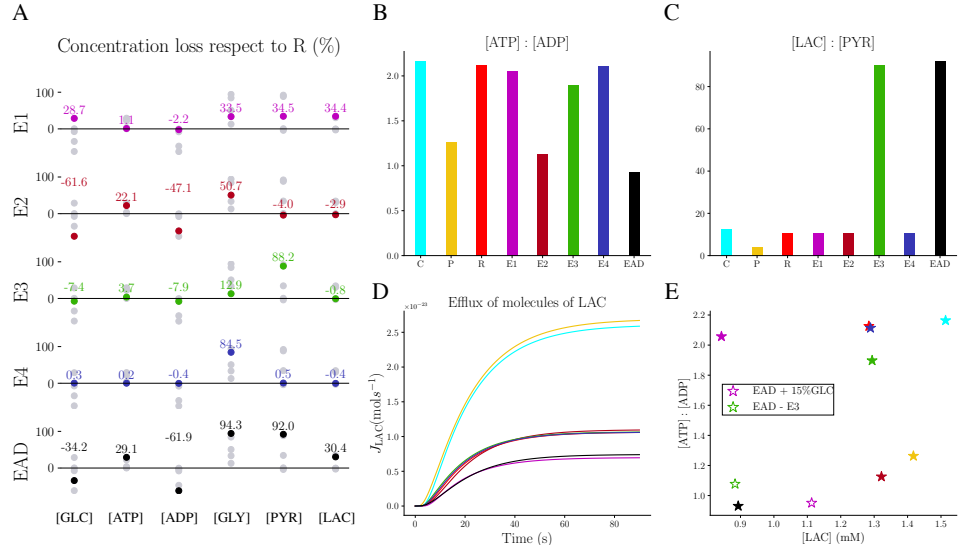
Fig 7. Metabolite dynamics in 3D astrocytes with physiological reaction site versus extreme polarised arrangements.

We consider four pathological conditions of AD, in the setting of the reactive astrocyte R. E1 describes the deficiency of GLC uptake (magenta); E2, the mitochondria dysfunction (dark red); E3, the LDH overwork (green); E4, PYRK overwork (blue) and EAD, the four conditions combined (black). A: Final average concentration loss with respect to R. The experiments reflect their loss/gain imposed on the cell through the conditions. Steady-state spatially averaged B: ATP : ADP ratio and C: LAC : PYR ratio of control (cyan), polarised (yellow), reactive (red) and all the AD experiments. D: Efflux of LAC molecules exported over time from the astrocyte to the extracellular space. The experiments with higher export are the two control astrocyte with C and P configurations. The experiments with a lower export are E1 with a loss in GLC uptake and EAD with the combination of the AD conditions. E: Scatter plot of ATP : ADP against LAC final average values. The most efficient cell is the control one. Then, the different AD conditions affect the cell status leading the reactive cell affected by all the AD conditions to an unhealthy state. In order to save the EAD cell, we increase the uptake of GLC up to 85% (white star with magenta edge), and the cell responds by using the more available fuel to produce more LAC. However, blocking the LDH overwork (white star with green edge) increases ATP : ADP and thereby rescues the astrocyte from the AD conditions.

can neither support neurons nor itself. Last, we studied how to support an AD-impacted astrocyte where the results of the individual conditions helped to disentangle the different effects. Importing more GLC (by increasing the uptake to 85% of the healthy control condition) turns the cell into a more altruistic state by using the additional fuel predominantly for LAC production. Blocking the excessive activity of LDH saves the cell from AD-related energy deprivation but with the cost of reduced LAC export.

To investigate the impact of diffusion limitation as an underlying mechanism in reactive astrocytes, Fig 8 illustrates the time evolution of the 3D distribution of concentrations for the healthy C and AD-related EAD condition considering the properties and spatial distribution of reaction sites (S1-S12 Movies). In particular, the trapping effect discussed above is highlighted in the reactive astrocytic morphology for ATP and PYR where branches exhibit a higher concentration variability.

To summarise, the physiologically realistic simulations reproduce important features of astrocytes in healthy and diseased conditions. The incorporation of real morphologies highlights cellular robustness against extreme enzymatic configurations. This is also seen for AD conditions, indicating the influence of the cellular domain on the metabolic state of the cell. In fact, a single AD characteristic does not lead to an unhealthy cell, only combinations of AD terrain lead to severe metabolic dysfunctions.

Discussion

Although the link between cellular morphology and metabolic activity might have implications for neurodegeneration including Parkinson's disease and Alzheimer's disease, our understanding of this connection remains imperfect due in part to experimental limitations. Moreover, the role played by astrocytic metabolism in neuronal support is an open discussion [49]. To address this challenge, we developed a multiscale model for energy metabolism in complex cellular domains with a specific focus on the intracellular spatial orchestration of astrocytes. To build the mathematical model, we first considered a single reaction site for each metabolic subpathway in a 2D circular geometry and validated the model in terms of physiological concentration
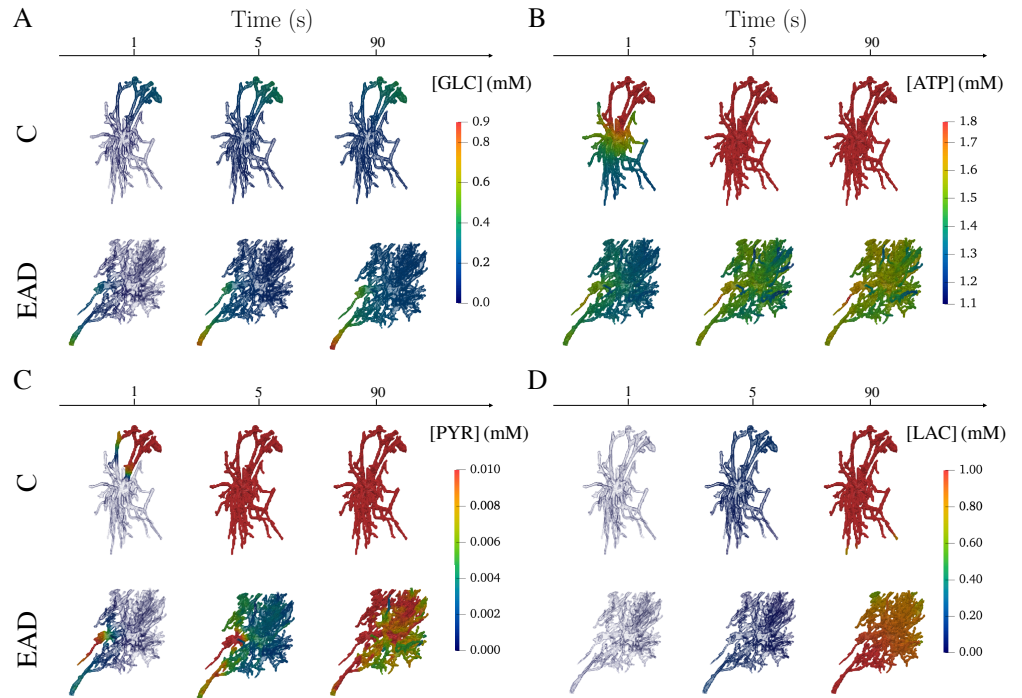
Fig 8. Spatially resolved Control and EAD astrocytes for GLC, ATP, PYR
and LAC **at different times.**
3D spatial concentration of metabolites at three different time steps in control (C) and
reactive astrocytes affected by AD pathology (EAD). A: GLC enters from the blood
vessels and spreads inside the astrocytic domains activating glucose metabolism. B:
ATP, already present in the cells at the initial time, is produced and consumed. In
particular, in correspondence with regions with high numbers/absence of Mito sites, we
can notice high/low levels of ATP in EAD. C: PYR produced by PYRK diffuses inside
the 3D domains and highlights the complex shape of the reactive astrocyte with high
variability of concentration within the cell. D: LAC shows a slow production, in fact at
time 5, both C and EAD show low concentrations. At the final time, we can appreciate
the steady state level of LAC where the regions where it is exported are highlighted by
lower concentrations.

ranges for astrocytes (Fig 1), in accordance with previous ODEs model [24]. We showed $_{417}$ numerically that different spatial organisations of reaction sites lead to distinct $_{418}$ metabolic profiles due to diffusion limitation and local substrate competition (Fig 2). $_{419}$ The observed differences between the circular and the star-shaped domain indicated a $_{420}$ possible trapping effect for molecules in more complex shapes. These trapping effects $_{421}$ might be overestimated compared to a more physiologically realistic astrocyte since $_{422}$ many more reaction sites are typically present within an astrocytic branch. $_{423}$ Nevertheless, these results strongly indicate that the spatial dimension and domain $_{424}$ complexity can have a crucial effect on metabolic profiles and may be of particular $_{425}$ importance for the metabolic support function of astrocytes. $_{426}$

To further characterise these spatial effects in a more physiological setting, we $_{427}$ considered a larger number of reaction sites, which were distributed either within a $_{428}$ uniform or polarised arrangement inside a rectangular shape, mimicking an astrocytic $_{429}$ branch. For each configuration, we ran 200 realisations, allowing for robust statistical $_{430}$ comparisons between the different settings (Fig 3). The results showed that cells with $_{431}$ uniformly distributed reaction sites are significantly more efficient in both the $_{432}$ "altruistic" LAC production as well as the "egocentric" intracellular energy state. $_{433}$ Although polarised organisation corresponds to an extreme and rare biological setting, $_{434}$ the analysis of these realisations indicates the importance of a more homogeneous $_{435}$ mitochondria distribution for sufficient activity and a related energised cell state (Fig 4). $_{436}$ This is in line with the experimental observation of mitochondrial organisation and $_{437}$ homeostasis including fission and fusion where impairment of these processes is linked $_{438}$ to neurodegeneration [50]. $_{439}$

Based on the 2D model, we extended our investigations to physiological 3D $_{440}$ morphologies of astrocytes, obtained from confocal microscopy images of human $_{441}$ *post-mortem* brain samples of an AD patient and a healthy control subject. Our $_{442}$ approach is thereby able to integrate directly the spatial orchestration of reaction $_{443}$ enzymes as demonstrated by the experimentally quantified mitochondrial distribution $_{444}$ (Fig 5). We first confirmed that using different morphologies but the same parameters $_{445}$ leads to concentrations in the physiological range in agreement with the findings in the $_{446}$ simplified 2D geometries (Fig 6). To investigate the effect of AD-related molecular $_{447}$ modifications, we analysed a reactive astrocyte with baseline parameters and four $_{448}$

individual metabolic dysfunctions linked to AD and their combinations (Fig 7). The   449
results highlighted that different pathological effects arouse specific system responses   450
and differentiated the cell behaviour between an "altruistic" and an "egocentric" mode.   451
Furthermore, the results indicated that any given dysfunction does not lead necessarily   452
to a dysfunctional cell with a low ATP : ADP ratio but it is the cumulative metabolic   453
insufficiencies that lead the cell into a critical state. This synergistic phenotype might   454
be related to the multi-hit perspective in neurodegeneration which addresses the   455
transient compensation and typical disease onset at higher age [51, 52]. The systematic   456
study of the individual dysfunctions allowed to suggest that reducing LDH activity   457
could sustain astrocytic function. Such approaches are also discussed in the context of   458
cancer [53, 54]. However, in the context of AD, the challenge would be to interfere with   459
metabolism in a cell-type-specific manner.   460

   The comparison between the simplified 2D domains and the complex 3D   461
morphologies indicates that real astrocytic shapes affect the cell state with robustness   462
towards enzyme orchestration and different metabolic dysfunctions. This robustness   463
might be caused by the trapping of molecules in thin branches as further indicated by   464
the analysis of 2D star-shaped morphology. The thin processes may hamper the   465
diffusion of molecules as shown by the spatial concentration profiles (Fig 8) which   466
increased mitochondrial activity and corresponding ATP production with the cost of   467
decreased LAC export. Thus, the complex morphology might provide a mechanism to   468
support an "egocentric" state if the system reaches limiting conditions, similar to energy   469
buffering in complex mitochondrial morphologies [55].   470

   While in literature several modelling approaches for metabolism have been proposed,   471
such as genome-scale modelling [21, 23, 56, 57] or more quantitative description via   472
kinetic models [58–60], we propose a metabolic model including molecular diffusivity   473
and spatial orchestraton of reaction sites. Furthermore, to our knowledge, our approach   474
is the first 3D model of cellular energy metabolism using physiological human cellular   475
morphologies. However, the crucial role of geometries has been taken into account in   476
other modelling such as for calcium signalling in astrocyte [61–63] further indicating the   477
importance of morphology. In agreement with these findings, our analyses of   478
hippocampal control and AD-related reactive astrocytes clearly demonstrate the   479
importance of morphology for cellular metabolic activity. While our studies refer to two   480

specific astrocytic morphologies, an AD and an aged-match control, our framework can be easily applied to each segmented astrocytic image and the crucial role of complex morphology is already visible in these experiments. Our approach has limitations, such as the lack of cellular compartmentalisation, the coarse-graining of enzymatic reaction into effective metabolic pathways, the limitation of the GFAP staining and the incomplete information on reaction site localisation provided by imaging modalities.

The model can be expanded by considering more detailed equations and including pyruvate exchanger with mitochondria, creatine phosphate shuttle or oxygen concentration. The more complex mathematical formulation of the model can integrate the inhibition of glycolysis in the presence of a high concentration of ATP [64], which would allow us to investigate better the energetic behaviour of astrocytes. Also, we could extend the experiment presented in S5 in S1 Text, considering the cellular activity consuming more ATP in the perisynaptic regions [2, 36]. Following the experiment presented in S5 in S1 Text, the regions exporting lactate can be defined better for example by investigating the distribution of lactate transporters via immunohistochemistry (IHC) images [65]. Furthermore, GFAP staining does not capture the full astrocytic morphology [31]. Comparison between GFAP staining and volumetric analyses by electron microscopic images (EM) have shown that volumes can differ by a factor of up to 1.5 which will particularly affect diffusion-mediated processes. This limitation can be addressed by appropriate scaling of the morphological reconstruction or adaptation of the diffusion coefficients. While such scaling may lead to minor quantitative changes in our analysis the qualitative findings will not be affected. This effect will be addressed in future investigations using 3D electron microscopic images which reconstruct astrocytic morphologies in more detail [66]. However, the images obtained by GFAP staining are suitable for creating finite element meshes, while EM images will require a more computationally demanding mesh construction. Concerning the computational model, a further step would be to ensure the accuracy of the solution by measuring the discretization error using real-time error estimation for biomedicine [67–70] or expanding the sensitivity analysis presented in S1 in S1 Text with detailed quantification analysis [71, 72].

Another important application of our approach will be the investigation of mitochondrial turnover and resulting distributions in astrocytes [73, 74]. Despite these

limitations, we demonstrate the general importance and feasibility of physiological $_{513}$
simulations by integrating molecular properties, spatial intracellular orchestration and $_{514}$
morphology. Even though we characterised our results on the average steady-state $_{515}$
concentration, further investigation can be done in subdomains as we showed for LAC $_{516}$
in Fig 7D. Based on our multiscale framework, future investigations will allow $_{517}$
disentangling different mechanisms underlying neurodegeneration, including $_{518}$
mitochondrial morphology [55, 75], organisation and dysfunction [76–78] by more $_{519}$
detailed models. $_{520}$

Materials and methods $_{521}$

Ethics Statement $_{522}$

Post-mortem brain tissue was obtained from the Douglas-Bell Canada Brain Bank and $_{523}$
handled according to the agreements with the Ethics Board of the Douglas-Bell Brain $_{524}$
Bank (Douglas Mental Health University Institute, Montréal, QC, Canada) and the $_{525}$
Ethic Panel of the University of Luxembourg (ERP 16-037 and 21-009). The two $_{526}$
hippocampal samples used in this work were donated from a male 87-year-old $_{527}$
Alzheimer's Disease patient with a disease stage of A2B3C2 and a post-mortem interval $_{528}$
of 21,75 hours, and by a female 89-year-old (age-matched) control subject with a $_{529}$
post-mortem interval of 23,58 hours. All donors gave their written consent. $_{530}$

Energy Metabolism Model $_{531}$

The core energy metabolism is broken down into the core metabolic pathways by the
coarse-grained non-reversible reactions:

$$\text{HXK} := \text{GLC} + 2\,\text{ATP} \rightarrow 2\,\text{ADP} + 2\text{GLY} \tag{1}$$

$$\text{PYRK} := \text{GLY} + 2\,\text{ADP} \rightarrow 2\,\text{ATP} + \text{PYR} \tag{2}$$

$$\text{LDH} := \text{PYR} \rightarrow \text{LAC} \tag{3}$$

$$\text{Mito} := \text{PYR} + 28\,\text{ADP} \rightarrow 28\,\text{ATP} \tag{4}$$

$$\text{act} := \text{ATP} \rightarrow \text{ADP} , \tag{5}$$

where the first two reactions consider the ATP-consuming and ATP-producing parts of glycolysis, LDH describes the activity of lactate dehydrogenase. Mito reflects the overall metabolic activity of mitochondria in terms of ATP production and general cellular activity is reflected by the act reaction.

Reaction Diffusion System

To investigate the spatial coupling of the metabolic pathways (Eqs. (1)-(5)), the reactions were integrated by a RDS [79]. The domain of the PDEs is a bounded subset of $\mathbb{R}^d$ ($d = 2$ or 3), denoted by Ω and concentrations $[\cdot]$ are defined as function $[\cdot] : \Omega \times [0, T] \to \mathbb{R}$. Diffusion coefficients for each species are given by $D_{[\cdot]}$ and chemical reactions are modelled using mass action kinetics [80]. The reaction rate for homogeneous cellular activity (K_{act}) and a spatial reaction rate density, $\mathcal{K}_j$, for the other four reactions. Considering M reaction sites located in $\{\mathbf{x}_i\}_{i=1}^{M} \in \Omega$, the spatial reaction rates are defined as the product between the classical reaction rates, K_j, and Gaussian functions located at those reaction sites with variance $\sigma_i \in \mathbb{R}^+$:

$$\mathcal{K}_j(\mathbf{x}) = \frac{K_j}{\xi} \mathrm{meas}(\Omega) \sum_{i=1}^{M} \mathcal{G}(\mathbf{x}_i, \sigma_i) \quad j = \{\mathrm{HXK}, \mathrm{PYRK}, \mathrm{Mito}, \mathrm{LDH}\}. \tag{6}$$

ξ is a parameter that ensure the property that $\int_{\Omega} \mathcal{K}_j \mathrm{d}x = K_j$ and $\mathrm{meas}(\Omega)$ is the area of the domain in 2D or the volume in 3D. The source of GLC is described through a function $J_{\mathrm{in}} : \Omega \times [0, T] \to \mathbb{R}$:

$$J_{\mathrm{in}}(x, t) = \begin{cases} \alpha \in \mathbb{R} & \text{if} \quad (x, t) \in \Omega_{\mathrm{in}} \times [0, T], \quad \text{where} \quad \Omega_{\mathrm{in}} \subset \Omega \\ 0 & \text{otherwise.} \end{cases} \tag{7}$$

Similarly, the degradation of LAC, which is proportional to the amount of LAC in region $\Omega_{\mathrm{out}} \subset \Omega$ is described by function $\eta_{\mathrm{LAC}} : \Omega \times [0, T] \to \mathbb{R}$

$$\eta_{\mathrm{LAC}}(x, t) = \begin{cases} \eta \in \mathbb{R} & \text{if} \quad (x, t) \in \Omega_{\mathrm{out}} \times [0, T], \quad \text{where} \quad \Omega_{\mathrm{out}} \subset \Omega \\ 0 & \text{otherwise.} \end{cases} \tag{8}$$

With this definition, the reaction-diffusion system is given by

$$\begin{cases} \frac{\partial[\mathrm{GLC}]}{\partial t} = & D_{[\mathrm{GLC}]}\nabla^2[\mathrm{GLC}] - \mathcal{K}_{\mathrm{HXK}}[\mathrm{GLC}][\mathrm{ATP}]^2 + J_{\mathrm{in}} \\[6pt] \frac{\partial[\mathrm{ATP}]}{\partial t} = & D_{[\mathrm{ATP}]}\nabla^2[\mathrm{ATP}] - 2\mathcal{K}_{\mathrm{HXK}}[\mathrm{GLC}][\mathrm{ATP}]^2 + 2\mathcal{K}_{\mathrm{PYRK}}[\mathrm{ADP}]^2[\mathrm{GLY}] \\[6pt] & +28\mathcal{K}_{\mathrm{Mito}}[\mathrm{PYR}][\mathrm{ADP}]^{28} - K_{\mathrm{act}}[\mathrm{ATP}] \\[6pt] \frac{\partial[\mathrm{ADP}]}{\partial t} = & D_{[\mathrm{ADP}]}\nabla^2[\mathrm{ADP}] + 2\mathcal{K}_{\mathrm{HXK}}[\mathrm{GLC}][\mathrm{ATP}]^2 - 2\mathcal{K}_{\mathrm{PYRK}}[\mathrm{ADP}]^2[\mathrm{GLY}] \\[6pt] & +K_{\mathrm{act}}[\mathrm{ATP}] - 28\mathcal{K}_{\mathrm{Mito}}[\mathrm{PYR}][\mathrm{ADP}]^{28} \\[6pt] \frac{\partial[\mathrm{GLY}]}{\partial t} = & D_{[\mathrm{GLY}]}\nabla^2[\mathrm{GLY}] + 2\mathcal{K}_{\mathrm{HXK}}[\mathrm{GLC}][\mathrm{ATP}]^2 - \mathcal{K}_{\mathrm{PYRK}}[\mathrm{ADP}]^2[\mathrm{GLY}] \\[6pt] \frac{\partial[\mathrm{PYR}]}{\partial t} = & D_{[\mathrm{PYR}]}\nabla^2[\mathrm{PYR}] + \mathcal{K}_{\mathrm{PYRK}}[\mathrm{ADP}]^2[\mathrm{GLY}] - \mathcal{K}_{\mathrm{LDH}}[\mathrm{PYR}] \\[6pt] & -\mathcal{K}_{\mathrm{Mito}}[\mathrm{PYR}][\mathrm{ADP}]^{28} \\[6pt] \frac{\partial[\mathrm{LAC}]}{\partial t} = & D_{[\mathrm{LAC}]}\nabla^2[\mathrm{LAC}] + \mathcal{K}_{\mathrm{LDH}}[\mathrm{PYR}] - \eta_{\mathrm{LAC}}[\mathrm{LAC}] \, , \end{cases} \tag{9}$$

where we considered Von Neumann boundary condition to consider no-flux settings at the cell membrane, in agreement with the impermeability of the cell membrane to these intermediates. To characterise the system's behavior, we analysed the equilibrating dynamics towards the steady state from the initial conditions for ATP and ADP concentrations

$$\begin{cases} [\mathrm{ATP}](x, t=0) \in \mathbb{R} & x \in \Omega \\[6pt] [\mathrm{ADP}](x, t=0) \in \mathbb{R} & x \in \Omega \end{cases}$$

where an initial ATP concentration is required for the initial glycolysis reactions and vanishing concentrations for the other species. To ensure robust simulations, we transformed the RDS into a dimensionless system allowing for convergence over a large parameter range (S8 in S1 Text).

Immunofluorescence stainings

The PFA-fixed hippocampal samples were cryosectioned into $50 - 100\,\mu$m thick slices on a sliding freezing microtome (Leica SM2010R). To visualise astrocytes and mitochondria, we co-immunostained the slices against glial fibrillary acidic protein (GFAP) and Tu translation elongation factor mitochondrial (TUFM) respectively. The target-binding primary antibodies used here were Anti-GFAP guinea-pig (Synaptic

Systems Cat# 173 004, RRID:AB_10641162) at a dilution of 1:500, and Anti-TUFM mouse (Atlas Antibodies Cat# AMAb90966, RRID:AB_2665738) at a dilution of 1 : 200. The corresponding fluorophore-coupled secondary antibodies used were Alexa Fluor 647-AffiniPure Donkey Anti-Guinea Pig IgG (H+L) (Jackson ImmunoResearch Labs Cat# 706-605-148, RRID:AB_2340476) at a dilution of 1 : 300 and Alexa Fluor 488-AffiniPure Donkey Anti-Mouse IgG (H+L) (Jackson ImmunoResearch Labs Cat# 715-545-150, RRID:AB_2340846) at a dilution of 1 : 400. We followed a previously published protocol [30] with the exception of a double incubation with primary antibodies for the TUFM staining.

Image acquisitions

High-resolution confocal images with $0.333\,\mu$m z-step were acquired using a Leica DMi8 microscope with a 93X glycerol objective and LAS X software (Leica Microsystems). The region of interest was fixed on the hippocampal subregion CA1.

Image pre-processing

The surface function of Imaris 9.6.0 software was used to segment GFAP staining to produce astrocyte morphology 3D reconstructions. The surface grain size parameter was set to $0.3\,\mu$m for the segmentation of astrocyte morphology. Upon segmentation of the GFAP signal of the entire image, we manually selected the astrocyte of interest and removed all other non-relevant segmentation structures. The spots function was used to segment TUFM staining. The estimated spots diameter was set to $0.2\,\mu$m. To select only the mitochondria of interest (corresponding to the astrocyte of interest) we applied the filter of the spots function called 'Shortest Distance to Surface' [segmented astrocyte]. In the control astrocyte, some mitochondria of interest were not automatically selected by this filter setting, because they were too far away from the segmented surface, however part of the astrocyte, notably in the cell soma. To include these mitochondria into the analysis, a second filter was applied twice by selecting the central mitochondria of the soma compartment and applying 'Shortest Distance to Surface' function.

The direct use of the astrocytic segmented images as domain for our simulation

would require a mesh fine enough to capture the thin branches of the cellular structure. 591
This would mean billions of quality finite elements, with a good aspect ratio. In 592
literature, this problem was addressed by refining the mesh in critical regions [81]. 593
However, in our case, this would require refining all branches. We overcome these issues 594
by additional image pre-processing where we dilated and down-sampled the binary 595
images. These two steps enlarged the thin branches and avoid discontinuities when we 596
map the images to the finite element mesh. These steps are not critically affecting the 597
real morphology of the astrocytes and might actually address partially the GFAP 598
staining limitation. Moreover, we impose the astrocytic volume in the simulations to be 599
equal to the one of the segmented images obtained with Imaris. Eventually, we obtained 600
the final segmented images (f) by labelling the voxels inside (-1), outside (1) and on 601
the boundary (0) of the astrocytes. 602

Before applying the same steps to the binarised segmented mitochondrial images, we 603
applied a convolution filter to smooth the voxels. To extrapolate the information about 604
mitochondrial density, we selected all connected components in the images and for each 605
of them, we identified the center and the radius of the circle that contains such 606
component. 607

Numerical methods 608

To solve numerically the RDS, the first step is to convert Eq. 9 into a corresponding 609
weak form [82]. Then, we discretise the weak form both in time and space. We discretise 610
the time derivative using a finite difference method (backward Euler) [83] and the 611
spatial domain by finite elements [84] and cut finite elements [85]. The 2D experiments 612
were solved using classical finite element methods based on FEniCS [86, 87], while the 613
3D experiments were solved using CutFEM [33, 85]. Since the weak RDS formulation is 614
non-linear, we linearised it and used a Newton-Raphson algorithm to iteratively solve 615
the problem. The linear system at each time step of the Newton-Raphson algorithm was 616
solved using standard linear solver from the *PETSc* library. For further details and 617
numerical parameters see S9, S10 and S11 in S1 Text, respectively. 618

Physiological model parameters

The parameters used in our model are given in Table 1. The diffusion parameters were chosen for ATP and ADP following [38], for GLC based on [37] and for the other species based on the Polson method [39, 40].

The calibration of the reaction rates has been done in accordance with the steady states of the ODE system [24] associated with Eq. (9). For J_{in} we used the maximum transport rate of GLC from [24]. For J_{out} we used the maximum transport rate of LAC but divided it for the steady state since we required our transport of LAC to be proportional to the local concentration of LAC inside the cell.

Data Availability

The code and data associated with the simulations are available at the following repository: GitLAB-energy-metabolism-model-astrocyte

Author contributions

Acknowledgements

References

1. Laughlin SB, de Ruyter van Steveninck RR, Anderson JC. The metabolic cost of neural information. Nature neuroscience. 1998;1(1):36–41.

2. Pellerin L, Magistretti PJ. Glutamate uptake into astrocytes stimulates aerobic glycolysis: a mechanism coupling neuronal activity to glucose utilization. Proceedings of the National Academy of Sciences. 1994;91(22):10625–10629.

3. Bélanger M, Allaman I, Magistretti PJ. Brain energy metabolism: focus on astrocyte-neuron metabolic cooperation. Cell metabolism. 2011;14(6):724–738. doi:10.1016/j.cmet.2011.08.016.

4. Patel AB, Lai JC, Chowdhury GM, Hyder F, Rothman DL, Shulman RG, et al. Direct evidence for activity-dependent glucose phosphorylation in neurons with implications for the astrocyte-to-neuron lactate shuttle. Proceedings of the National Academy of Sciences. 2014;111(14):5385–5390.

5. Patsatzis DG, Tingas EA, Goussis DA, Sarathy SM. Computational singular perturbation analysis of brain lactate metabolism. PloS one. 2019;14(12):e0226094.

6. Escartin C, Galea E, Lakatos A, O'Callaghan JP, Petzold GC, Serrano-Pozo A, et al. Reactive astrocyte nomenclature, definitions, and future directions. Nature neuroscience. 2021;24(3):312–325.

7. Bouvier DS, Fixemer S, Heurtaux T, Jeannelle F, Frauenknecht K, Mittelbronn M. The Multifaceted Neurotoxicity of Astrocytes in Ageing and Age-Related Neurodegenerative Diseases: A Translational Perspective. Frontiers in Physiology. 2022; p. 467.

8. Pekny M, Pekna M. Astrocyte reactivity and reactive astrogliosis: costs and benefits. Physiological reviews. 2014;94(4):1077–1098.

9. Bouvier DS, Jones EV, Quesseveur G, Davoli MA, A Ferreira T, Quirion R, et al. High resolution dissection of reactive glial nets in Alzheimer's disease. Scientific reports. 2016;6(1):1–15.

10. Wilhelmsson U, Bushong EA, Price DL, Smarr BL, Phung V, Terada M, et al. Redefining the concept of reactive astrocytes as cells that remain within their unique domains upon reaction to injury. Proceedings of the National Academy of Sciences. 2006;103(46):17513–17518.

11. Acaz-Fonseca E, Ortiz-Rodriguez A, Azcoitia I, Garcia-Segura LM, Arevalo MA. Notch signaling in astrocytes mediates their morphological response to an inflammatory challenge. Cell death discovery. 2019;5(1):85.

12. Bigl M, Brückner M, Arendt T, Bigl V, Eschrich K. Activities of key glycolytic enzymes in the brains of patients with Alzheimer's disease. Journal of neural transmission. 1999;106(5):499–511.

13. Camandola S, Mattson MP. Brain metabolism in health, aging, and neurodegeneration. The EMBO journal. 2017;36(11):1474–1492.

14. Arranz AM, De Strooper B. The role of astroglia in Alzheimer's disease: pathophysiology and clinical implications. The Lancet Neurology. 2019;doi:10.1016/S1474-4422(18)30490-3.

15. Cotto B, Natarajaseenivasan K, Langford D. Astrocyte activation and altered metabolism in normal aging, age-related CNS diseases, and HAND. Journal of neurovirology. 2019;25(5):722–733.

16. Zulfiqar S, Garg P, Nieweg K. Contribution of astrocytes to metabolic dysfunction in the Alzheimer's disease brain. Biological chemistry. 2019;400(9):1113–1127.

17. Schurr A, West CA, Rigor BM. Lactate-supported synaptic function in the rat hippocampal slice preparation. Science. 1988;240(4857):1326–1328.

18. Tantama M, Yellen G. Imaging changes in the cytosolic ATP-to-ADP ratio. In: Methods in enzymology. vol. 547. Elsevier; 2014. p. 355–371.

19. Tantama M, Martínez-François JR, Mongeon R, Yellen G. Imaging energy status in live cells with a fluorescent biosensor of the intracellular ATP-to-ADP ratio. Nature communications. 2013;4(1):1–11.

20. Magistretti PJ, Allaman I. Lactate in the brain: from metabolic end-product to signalling molecule. Nature Reviews Neuroscience. 2018;19(4):235–249.

21. Martín-Jiménez CA, Salazar-Barreto D, Barreto GE, González J. Genome-scale reconstruction of the human astrocyte metabolic network. Frontiers in aging neuroscience. 2017;9:23.

22. Berndt N, Bulik S, Holzhütter HG. Kinetic modeling of the mitochondrial energy metabolism of neuronal cells: the impact of reduced-ketoglutarate dehydrogenase activities on ATP production and generation of reactive oxygen species. International journal of cell biology. 2012;2012.

23. Çakır T, Alsan S, Saybaşılı H, Akın A, Ülgen KÖ. Reconstruction and flux analysis of coupling between metabolic pathways of astrocytes and neurons: application to cerebral hypoxia. Theoretical Biology and Medical Modelling. 2007;4(1):48. doi:10.1186/1742-4682-4-48.

24. Cloutier M, Bolger FB, Lowry JP, Wellstead P. An integrative dynamic model of brain energy metabolism using in vivo neurochemical measurements. Journal of computational neuroscience. 2009;27(3):391. doi:10.1007/s10827-009-0152-8.

25. Sertbaş M, Ülgen K, Çakır T. Systematic analysis of transcription-level effects of neurodegenerative diseases on human brain metabolism by a newly reconstructed brain-specific metabolic network. FEBS Open Bio. 2014;4:542–553. doi:https://doi.org/10.1016/j.fob.2014.05.006.

26. Jolivet R, Coggan JS, Allaman I, Magistretti PJ. Multi-timescale modeling of activity-dependent metabolic coupling in the neuron-glia-vasculature ensemble. PLoS computational biology. 2015;11(2):e1004036.

27. Coggan JS, Keller D, Calì C, Lehväslaiho H, Markram H, Schürmann F, et al. Norepinephrine stimulates glycogenolysis in astrocytes to fuel neurons with lactate. PLoS computational biology. 2018;14(8):e1006392.

28. Sánchez-Alvarez R, Tabernero A, Medina JM. Endothelin-1 stimulates the translocation and upregulation of both glucose transporter and hexokinase in

astrocytes: relationship with gap junctional communication. Journal of neurochemistry. 2004;89(3):703–714.

29. Jackson JG, Robinson MB. Regulation of mitochondrial dynamics in astrocytes: Mechanisms, consequences, and unknowns. Glia. 2018;66(6):1213–1234.

30. Quesseveur G, d'Hérouël AF, Murai KK, Bouvier DS. A specialized method to resolve fine 3D features of astrocytes in nonhuman primate (marmoset, Callithrix jacchus) and human fixed brain samples. In: Benedetto BD, editor. Astrocytes. Regensburg, Germany: Springer; 2019. p. 85–95.

31. Bushong EA, Martone ME, Jones YZ, Ellisman MH. Protoplasmic astrocytes in CA1 stratum radiatum occupy separate anatomical domains. Journal of Neuroscience. 2002;22(1):183–192.

32. Farina S, Claus S, Hale JS, Skupin A, Bordas SP. A cut finite element method for spatially resolved energy metabolism models in complex neuro-cell morphologies with minimal remeshing. Advanced Modeling and Simulation in Engineering Sciences. 2021;8(1):1–32.

33. Burman E, Claus S, Hansbo P, Larson MG, Massing A. CutFEM: discretizing geometry and partial differential equations. International Journal for Numerical Methods in Engineering. 2015;104(7):472–501. doi:10.1002/nme.4823.

34. Claus S, Bigot S, Kerfriden P. CutFEM Method for Stefan–Signorini Problems with Application in Pulsed Laser Ablation. SIAM Journal on Scientific Computing. 2018;40(5):B1444–B1469. doi:10.1137/18M1185697.

35. Oberheim NA, Takano T, Han X, He W, Lin JH, Wang F, et al. Uniquely hominid features of adult human astrocytes. Journal of Neuroscience. 2009;29(10):3276–3287.

36. Winkler U, Seim P, Enzbrenner Y, Köhler S, Sicker M, Hirrlinger J. Activity-dependent modulation of intracellular ATP in cultured cortical astrocytes. Journal of neuroscience research. 2017;95(11):2172–2181.

37. Stein WD, Litman T. Channels, carriers, and pumps: an introduction to membrane transport. Elsevier; 2014.

38. Saks V, Kuznetsov A, Andrienko T, Usson Y, Appaix F, Guerrero K, et al. Heterogeneity of ADP diffusion and regulation of respiration in cardiac cells. Biophysical Journal. 2003;84(5):3436–3456.

39. Polson A. The Some Aspects of Diffusion in Solution and a Definition of a Colloidal Particle. The Journal of Physical Chemistry. 1950;54(5):649–652.

40. Tyn MT, Gusek TW. Prediction of diffusion coefficients of proteins. Biotechnology and bioengineering. 1990;35(4):327–338.

41. John S, Weiss JN, Ribalet B. Subcellular localization of hexokinases I and II directs the metabolic fate of glucose. PloS one. 2011;6(3):e17674.

42. Lynch RM, Fogarty KE, Fay FS. Modulation of hexokinase association with mitochondria analyzed with quantitative three-dimensional confocal microscopy. The Journal of cell biology. 1991;112(3):385–395.

43. Halassa MM, Fellin T, Takano H, Dong JH, Haydon PG. Synaptic islands defined by the territory of a single astrocyte. Journal of Neuroscience. 2007;27(24):6473–6477.

44. Bergersen LH. Lactate transport and signaling in the brain: potential therapeutic targets and roles in body—Brain interaction. Journal of Cerebral Blood Flow & Metabolism. 2015;35(2):176–185.

45. Mulica P, Grünewald A, Pereira SL. Astrocyte-Neuron Metabolic Crosstalk in Neurodegeneration: A Mitochondrial Perspective. Frontiers in Endocrinology. 2021;12.

46. Lin MT, Beal MF. Mitochondrial dysfunction and oxidative stress in neurodegenerative diseases. Nature. 2006;443(7113):787–795.

47. Motori E, Puyal J, Toni N, Ghanem A, Angeloni C, Malaguti M, et al. Inflammation-induced alteration of astrocyte mitochondrial dynamics requires autophagy for mitochondrial network maintenance. Cell metabolism. 2013;18(6):844–859.

48. Picone P, Nuzzo D, Caruana L, Scafidi V, Di Carlo M. Mitochondrial dysfunction: different routes to Alzheimer's disease therapy. Oxidative medicine and cellular longevity. 2014;2014.

49. Magistretti PJ, Allaman I. A cellular perspective on brain energy metabolism and functional imaging. Neuron. 2015;86(4):883–901.

50. Liu YJ, McIntyre RL, Janssens GE, Houtkooper RH. Mitochondrial fission and fusion: A dynamic role in aging and potential target for age-related disease. Mechanisms of ageing and development. 2020;186:111212.

51. Patrick KL, Bell SL, Weindel CG, Watson RO. Exploring the "multiple-hit hypothesis" of neurodegenerative disease: bacterial infection comes up to bat. Frontiers in Cellular and Infection Microbiology. 2019;9:138.

52. Zhu X, Lee Hg, Perry G, Smith MA. Alzheimer disease, the two-hit hypothesis: an update. Biochimica et Biophysica Acta (BBA)-Molecular Basis of Disease. 2007;1772(4):494–502.

53. Kim EY, Chung TW, Han CW, Park SY, Park KH, Jang SB, et al. A novel lactate dehydrogenase inhibitor, 1-(phenylseleno)-4-(trifluoromethyl) benzene, suppresses tumor growth through apoptotic cell death. Scientific reports. 2019;9(1):1–12.

54. Granchi C, Bertini S, Macchia M, Minutolo F. Inhibitors of lactate dehydrogenase isoforms and their therapeutic potentials. Current medicinal chemistry. 2010;17(7):672–697.

55. Garcia GC, Bartol TM, Phan S, Bushong EA, Perkins G, Sejnowski TJ, et al. Mitochondrial morphology provides a mechanism for energy buffering at synapses. Scientific reports. 2019;9(1):1–12.

56. Lee JM, Gianchandani EP, Papin JA. Flux balance analysis in the era of metabolomics. Briefings in bioinformatics. 2006;7(2):140–150.

57. Raman K, Chandra N. Flux balance analysis of biological systems: applications and challenges. Briefings in bioinformatics. 2009;10(4):435–449.

58. Aubert A, Costalat R. Interaction between astrocytes and neurons studied using a mathematical model of compartmentalized energy metabolism. Journal of Cerebral Blood Flow & Metabolism. 2005;25(11):1476–1490.

59. Aubert A, Costalat R, Magistretti PJ, Pellerin L. Brain lactate kinetics: modeling evidence for neuronal lactate uptake upon activation. Proceedings of the National Academy of Sciences. 2005;102(45):16448–16453.

60. Jolivet R, Magistretti PJ, Weber B. Deciphering neuron-glia compartmentalization in cortical energy metabolism. Frontiers in neuroenergetics. 2009;1:4.

61. Khalid MU, Tervonen A, Korkka I, Hyttinen J, Lenk K. Geometry-based computational modeling of calcium signaling in an astrocyte. In: Eskola H, Väisänen O, Viik J, Hyttinen J, editors. EMBEC & NBC 2017. Singapore: Springer Singapore; 2017. p. 157–160.

62. Denizot A, Arizono M, Nägerl UV, Soula H, Berry H. Simulation of calcium signaling in fine astrocytic processes: Effect of spatial properties on spontaneous activity. PLoS computational biology. 2019;15(8):e1006795.

63. Verisokin AY, Verveyko DV, Postnov DE, Brazhe AR. Modeling of astrocyte networks: toward realistic topology and dynamics. Frontiers in Cellular Neuroscience. 2021;15:645068.

64. Maldonado EN, Lemasters JJ. ATP/ADP ratio, the missed connection between mitochondria and the Warburg effect. Mitochondrion. 2014;19:78–84.

65. Hashimoto T, Masuda S, Taguchi S, Brooks GA. Immunohistochemical analysis of MCT1, MCT2 and MCT4 expression in rat plantaris muscle. The Journal of physiology. 2005;567(1):121–129.

66. Calì C, Agus M, Kare K, Boges DJ, Lehväslaiho H, Hadwiger M, et al. 3D cellular reconstruction of cortical glia and parenchymal morphometric analysis from Serial Block-Face Electron Microscopy of juvenile rat. Progress in neurobiology. 2019;183:101696.

67. Bordas S, Bucki M, Chouly F, Duprez M, Lleras V, Lobos C, et al. Quantifying discretization errors for soft-tissue simulation in computer assisted surgery: a preliminary study. 2017;.

68. Bui HP, Tomar S, Courtecuisse H, Cotin S, Bordas SP. Real-time error control for surgical simulation. IEEE Transactions on Biomedical Engineering. 2017;65(3):596–607. doi:10.1109/TBME.2017.2695587.

69. Duprez M, Bordas S, Bucki M, Bui HP, Chouly F, Lleras V, et al. Quantifying discretization errors for soft-tissue simulation in computer assisted surgery: a preliminary study. arXiv preprint arXiv:180606944. 2018;doi:10.1016/j.apm.2019.07.055.

70. Bui HP, Tomar S, Courtecuisse H, Audette M, Cotin S, Bordas SP. Controlling the error on target motion through real-time mesh adaptation: Applications to deep brain stimulation. International journal for numerical methods in biomedical engineering. 2018;34(5):e2958. doi:10.1002/cnm.2958.

71. Hauseux P, Hale JS, Cotin S, Bordas SP. Quantifying the uncertainty in a hyperelastic soft tissue model with stochastic parameters. Applied Mathematical Modelling. 2018;62:86–102. doi:10.1016/j.apm.2018.04.021.

72. Rappel H, Beex L. Estimating fibres' material parameter distributions from limited data with the help of Bayesian inference. European Journal of Mechanics-A/Solids. 2019;75:169–196. doi:10.1016/j.euromechsol.2019.01.001.

73. Goebel J, Engelhardt E, Pelzer P, Sakthivelu V, Jahn HM, Jevtic M, et al. Mitochondria-ER contacts in reactive astrocytes coordinate local perivascular domains to promote vascular remodelling. bioRxiv. 2020; p. 657999.

74. Salmon CK, Syed TA, Kacerovsky JB, Alivodej N, Schober AL, Pratte MT, et al. Organizing Principles of Astrocytic Nanoarchitecture in the Mouse Cerebral Cortex. bioRxiv. 2021;.

75. Siegmund SE, Grassucci R, Carter SD, Barca E, Farino ZJ, Juanola-Falgarona M, et al. Three-dimensional analysis of mitochondrial crista ultrastructure in a

patient with Leigh syndrome by in situ cryoelectron tomography. Iscience. 2018;6:83–91.

76. Johri A, Beal MF. Mitochondrial dysfunction in neurodegenerative diseases. Journal of Pharmacology and Experimental Therapeutics. 2012;342(3):619–630.

77. Soman S, Keatinge M, Moein M, Da Costa M, Mortiboys H, Skupin A, et al. Inhibition of the mitochondrial calcium uniporter rescues dopaminergic neurons in pink1-/- zebrafish. European Journal of Neuroscience. 2017;45(4):528–535.

78. Devine MJ, Kittler JT. Mitochondria at the neuronal presynapse in health and disease. Nature Reviews Neuroscience. 2018;19(2):63–80.

79. Murray JD. Mathematical biology: I. An introduction. vol. 17. Springer Science & Business Media; 2007.

80. Waage P, Gulberg CM. Studies concerning affinity. Journal of chemical education. 1986;63(12):1044. doi:10.1021/ed063p1044.

81. Claus S, Kerfriden P, Moshfeghifar F, Darkner S, Erleben K, Wong C. Contact modeling from images using cut finite element solvers. Advanced Modeling and Simulation in Engineering Sciences. 2021;8(1):1–23.

82. Brenner S, Scott R. The Mathematical Theory of Finite Element Methods. 3rd ed. Texts in Applied Mathematics. New York: Springer-Verlag; 2008. Available from: `https://www.springer.com/gp/book/9780387759333`.

83. Quarteroni A, Valli A. Numerical approximation of partial differential equations. Heidelberg: Springer Science & Business Media; 2008.

84. Hughes TJ. The finite element method: linear static and dynamic finite element analysis. Courier Corporation; 2012.

85. Bordas S, Menk A. Xfem: The Extended Finite Element Method. John Wiley; 2014.

86. Logg A, Mardal KA, Wells G. Automated solution of differential equations by the finite element method: The FEniCS book. Heidelberg: Springer Science & Business Media; 2012.

87. Alnæs MS, Blechta J, Hake J, Johansson A, Kehlet B, Logg A, et al. The FEniCS project version 1.5. Archive of Numerical Software. 2015;3(100):9–23. doi:10.11588/ans.2015.100.20553.

S1 Text Contents

S1: Stability analysis

S2: Spatial arrangements for 2D simulations in retangular shape

S3: Significance test for 2D realisation

S4: Local behaviour of ATP, ADP and PYR in maximum and minimum energised reaction site settings

S5: Simulating higher cellular activity in the perisynapses and more lactate efflux loci

S6: Spatial arrangement for 3D simulations

S7: Additional Figure for AD simulations

S8: Dimensionless system

S9: Detail on numerical methods for 2D simulations

S10: Details on numerical methods for 3D simulations

S11: Numerical Parameters

Supporting Movie Contents

S1 Movie: GLC control (C) astrocyte

S2 Movie: ATP control (C) astrocyte

S3 Movie: ADP control (C) astrocyte

S4 Movie: GLY control (C) astrocyte

S5 Movie: PYR control (C) astrocyte

S6 Movie: LAC control (C) astrocyte

S7 Movie: GLC reactive (EAD) astrocyte

S8 Movie: ATP reactive (EAD) astrocyte

S9 Movie: ADP reactive (EAD) astrocyte

S10 Movie: GLY reactive (EAD) astrocyte

S11 Movie: PYR reactive (EAD) astrocyte

S12 Movie: LAC reactive (EAD) astrocyte